

Article

Hot Deformation Behavior of Electron-Beam Cold-Hearth Melted Ti-6Al-4V Alloy

Weiju Jia ^{*} , Chengliang Mao and Wei Zhou

Northwest Institute for Nonferrous Metal Research, Xi'an 710016, China; mcl827@c-nin.com (C.M.); zw2021@c-nin.com (W.Z.)

* Correspondence: jwj1025@c-nin.com; Tel.: +86-29-86231078; Fax: +86-29-86231078

Abstract: The deformation behavior and microstructure changes of electron-beam cold-hearth-melted (EBCHM) Ti-6Al-4V alloy were investigated. The stress–strain curves of the alloy were obtained, the constitutive model was established based on the Arrhenius equation, and the hot processing map was drawn. The results showed that the stress of the alloy decreases with increasing temperature and decreasing strain rate. In the β phase field, there are more recrystallized grains when the strain rate is slow, and the recrystallization of the β phase does not have enough time to occur when the strain rate is fast. There are obvious shear bands in the microstructure at the strain rate of 10 s^{-1} . In the $\alpha + \beta$ field, the morphology and crystallographic orientation of the microstructure changed simultaneously. Globularization is a typical microstructure evolution characteristic. The prismatic slip is easier to activate than basal and pyramidal slips. Moreover, globularization of the lamellar α phase is not synchronously crystallographic and morphological.

Keywords: titanium alloy; electron-beam cold-hearth melting (EBCHM); hot deformation; microstructures

1. Introduction

Titanium alloys have been widely used in many industries due to their excellent strength-to-weight ratio and corrosion resistance [1,2]. Vacuum arc remelting (VAR) is the conventional melting method and is a widely used technology for titanium alloys. However, there are several possible problems during VAR melting, such as the inhomogeneity of the microstructure and composition, and low- and high-density inclusions [3,4]. Furthermore, with further application of titanium alloys in the marine, chemical, and equipment fields, the specification of the components become larger and larger, and the corresponding specification of single ingot also increasing. Larger ingots will lead to more obvious defects, as mentioned above. Electron-beam cold-hearth melting (EBCHM) is an effective process used to eliminate high- and low-density inclusions during melt processing, and to reduce the number of remelting steps for high quality titanium alloys. In addition, there is also a greater flexibility in the ingot form (cylinder or slab) in terms of the cross-section geometry of the water-cooled crystallizer and the ingot length depending on the adequate continuously withdrawing operations [5].

Ti-6Al-4V alloy is the most used titanium alloy. Usually, the alloy is melted by VAR and then forged to make the semi-finish products, and then at last forged or rolled to the final products. In recent years, there has been an increasing demand for large Ti-6Al-4V plates and strips, while requiring a low manufacturing cost for these products. EBCHM shows an advantage over VAR in manufacturing low-cost and large-specification products. The relationship between the process, microstructure, and properties of the VAR Ti-6Al-4V alloy has been extensively studied. In particular, the hot deformation behavior of the alloy under various conditions was studied [6–8]. However, limited research works have been performed for the EBCHM Ti-6Al-4V alloy. Despite the potential of the EBCHM process, the hot deformation behavior and microstructure characterization from this method have



Citation: Jia, W.; Mao, C.; Zhou, W. Hot Deformation Behavior of Electron-Beam Cold-Hearth Melted Ti-6Al-4V Alloy. *Metals* **2024**, *14*, 1459. <https://doi.org/10.3390/met14121459>

Academic Editor: Alain Pasturel

Received: 15 November 2024

Revised: 6 December 2024

Accepted: 12 December 2024

Published: 20 December 2024



Copyright: © 2024 by the authors. Licensee MDPI, Basel, Switzerland. This article is an open access article distributed under the terms and conditions of the Creative Commons Attribution (CC BY) license (<https://creativecommons.org/licenses/by/4.0/>).

not been established to any great extent. The traditional hot deformation behavior of titanium alloys provides guidance for the research in this work. The Arrhenius model is the most common constitutive model construction method, and it has been applied to a variety of titanium alloys, such as Ti-6Al-4V alloy [9], IMI834 alloy [10], Ti55531 alloy [11], DsTi700 [12], etc.

Microstructure evolution during high-temperature deformation is another area of concern because microstructure evolution determines the mechanical properties of the material. Globularization of the α phase is an important characteristic of microstructure evolution, and relevant studies have been carried out for different titanium alloys [13–17]. Balachandran et al. [18] found that the globularization and epitaxial recrystallization of the α phase are the main characteristics of microstructure evolution for Ti5553 alloy during hot deformation in the two-phase region. Xu et al. [19,20] studied the static globularization behavior of Ti17 alloy, established the kinetic model of globularization, and clarified the globularization mechanism. Previous research can help us to carry out the research work in this project.

In this work, the deformation behavior and microstructure evolution of EBCHM Ti-6Al-4V alloy during hot compression can provide guidance to produce Ti-6Al-4V. For instance, stress level and temperature increases under different conditions can guide the selection of processes for rotation speed and jacking force during cross-piercing. Microstructure evolution, such as grain size, recrystallization extent, grain boundary curvature, and so on, can help us set the right temperature of deformation. Hence, this study about the deformation behavior and microstructure evolution of EBCHM Ti-6Al-4V alloy is very meaningful for ensuring the high quality of Ti-6Al-4V final components.

The objective of this work is to study the high-temperature deformation behavior and microstructure changes of EBCHM Ti-6Al-4V alloy. For this purpose, the hot compression tests were conducted in single β and ($\alpha + \beta$) two-phase regions. High-temperature deformation behavior was analyzed via stress–strain curves, while the microstructure morphology was characterized by the optical microscope (OM) and electron back-scattered diffraction (EBSD) techniques.

2. Experimental Procedures

The material used in this work was received in bulk form with dimensions of $120 \times 150 \times 300$ mm, which was machined from a EBCHM Ti-6Al-4V ingot. The chemical composition of the as-received EBCHM Ti-6Al-4V alloy was analyzed by chemical methods and listed in Table 1. The β transus temperature was 980 °C, which was determined by using the metallographic method. The initial microstructure of the as-received EBCHM Ti-6Al-4V alloy is shown in Figure 1, and it presents a typical characterization of the casting microstructure containing large beta grains.

In the present work, the specimens with dimensions of $\Phi 10 \times 15$ mm were prepared for high-temperature compression tests. The Gleeble3500 thermo-simulator system was used to carry out compression tests. Hot compression tests were carried out in the temperature range of 910 – 1060 °C with 30 °C intervals and a strain rate range of 10^{-3} – 10 s $^{-1}$ on a Gleeble3500 simulator. The height reduction in the specimens was 65%. The specimens were heated to experimental temperatures with a heating rate of 5 °C/s and held for 5 min to ensure uniform temperature distribution. To reduce die friction and obtain uniform deformation, the ends of the specimens were coated with graphite powder, and a foil of tantalum was placed between the faces of the specimen and the anvils. During compression, temperature was monitored by a thermocouple which was welded in the center of the surface of the specimen. After deformation, the specimens were water-quenched immediately to preserve their microstructures at high temperatures.

Deformed specimens were sectioned parallel to the compression axis and prepared for metallographic examination using standard procedures. The $1/2$ radius of the specimens was chosen to observe microstructure changes. Finally, the OM and EBSD technologies were used for evaluating the microstructural evolution. In the EBSD tests, the step size was

set as 0.3 μm , and the other parameters were the system defaults. The EBSD data were analyzed using Channel 5 software.

Table 1. The chemical composition of the EBCHM Ti-6Al-4V alloy (wt %).

Al	V	Fe	C	H	N	O	Ti
6.21	4.31	0.172	0.009	0.0008	<0.003	0.12	Balanced

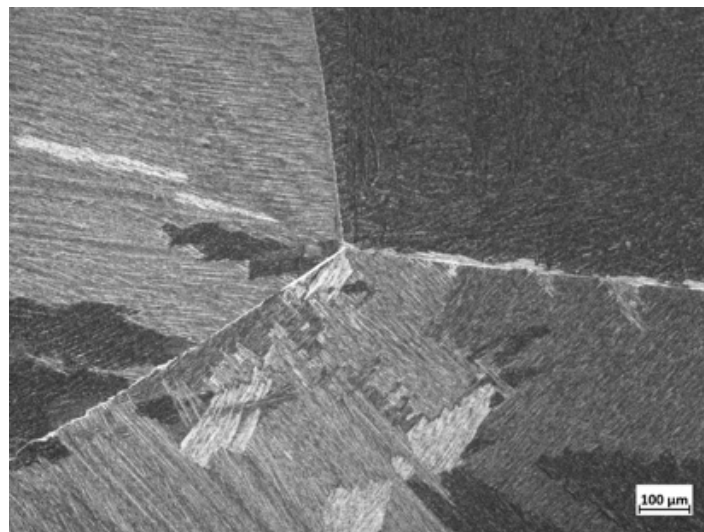


Figure 1. Initial microstructures of the EBCHM Ti-6Al-4V alloy.

3. Results and Discussion

3.1. Stress–Strain Curves

Figure 2 shows the stress–strain curves of EBCHM Ti-6Al-4V alloy deformed at 910 °C, 970 °C, 1030 °C, and 1060 °C. The first two represent the deformation behavior of the alloy in the ($\alpha + \beta$) two-phase region, while the last two represent the deformation behavior in the single β phase region. The curves indicate that the flow stress increases with increasing strain rate and decreasing temperature, showing a high sensitivity to strain rate and temperature. From the overall change trends, it can be seen that both in the ($\alpha + \beta$) phase region and single β phase region, basically, the flow stress reaches a steady state soon after arriving at the peak value. This type of flow curve, defined as a steady-state curve, usually means that the dynamic recovery (DRV), which can reduce the density of dislocation, will be the dominant softening behavior during the deformation [21]. However, some different flow curves can be observed in several deformation conditions in the ($\alpha + \beta$) two-phase region. When deformed at 910 °C with a low strain rate of 0.01–0.001 s^{-1} , the flow stress continues to decrease after the peak until it reaches a steady state. Moreover, when deformed at 970 °C with a high strain rate of 10 s^{-1} , the decrease in flow stress remains to the end of the deformation. The continuous dynamic flow softening characteristic indicates the possible occurrence of dynamic recrystallization (DRX) or the globularization of the lamellar α phase [22,23].

Based on the stress–strain curve, the deformation mechanism of the alloy can only be roughly speculated upon. Since the same variation trend of the flow curve may be caused by several different deformation mechanisms, in order to understand which mechanisms are involved in the deformation process of the alloy, it is necessary to use theoretical calculation and deformation microstructure analysis for a deeper understanding.

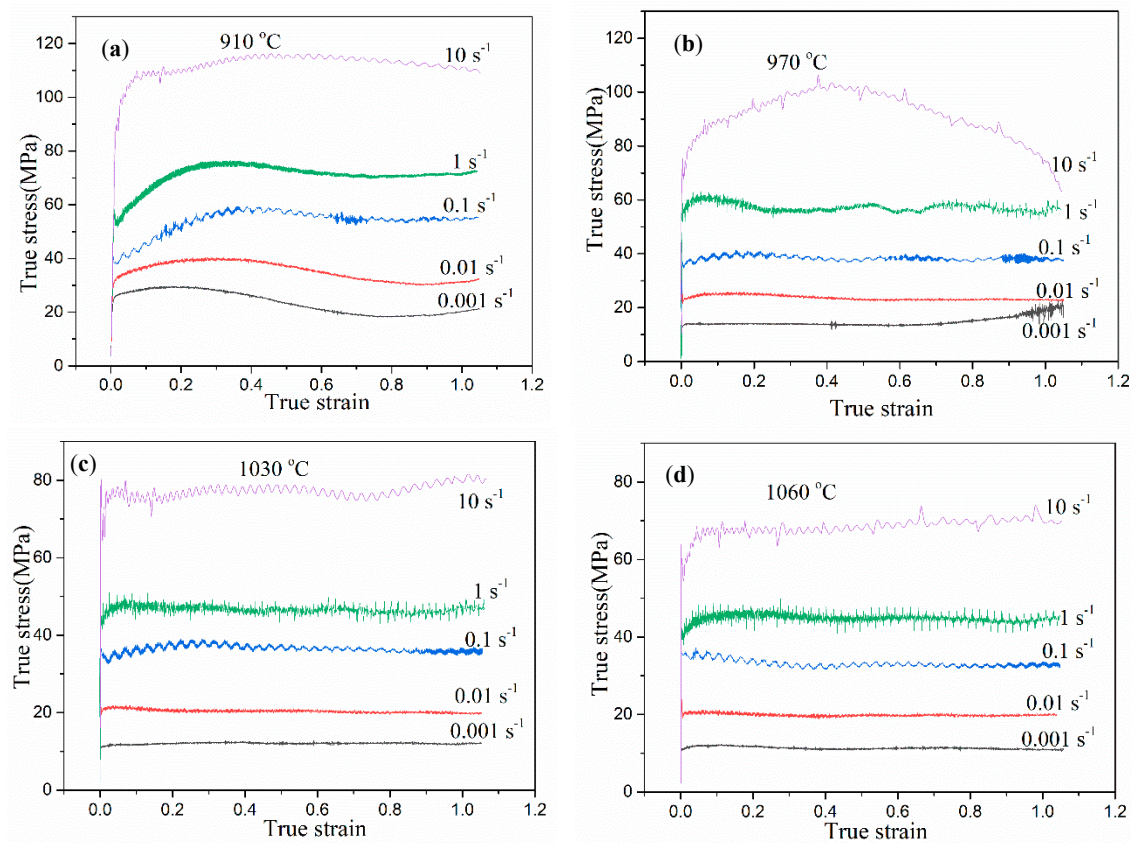


Figure 2. The stress–strain curves of the EBCHM Ti-6Al-4V alloy deformed at different temperatures: (a) 910 °C, (b) 970 °C, (c) 1030 °C, and (d) 1060 °C.

3.2. Constitutive Equation

From the point of deformation kinetics, the high-temperature plastic deformation of metal materials involves several thermal activation processes. Since the activation energies (Q) of different deformation mechanisms exhibit obvious differences, a reasonable estimate of the dominant deformation mechanism in the process of hot deformation can be made according to the calculated value of the apparent activation energy. Usually, the value of the apparent activation energy can be obtained by constructing the constitutive equation during the hot deformation, which can also visually express the relationship of the flow stress, deformation temperature, and strain rate. In this study, the classical Arrhenius equation was used to establish the constitutive model, which was expressed as follows [24]:

$$\text{When } \alpha\sigma < 0.8, \dot{\varepsilon} = A_1 e^{-\frac{Q}{RT}} \sigma^{n_1} \quad (1)$$

$$\text{When } \alpha\sigma > 1.2, \dot{\varepsilon} = A_2 e^{-\frac{Q}{RT}} \sigma^{\beta\sigma} \quad (2)$$

$$\text{For all } \sigma, \dot{\varepsilon} = A [\sinh(\alpha\sigma)]^n e^{-\frac{Q}{RT}} \quad (3)$$

where A_1 , A_2 , A , α (MPa^{-1}), and β are the temperature-independent material constants, n_1 and n are the stress exponent, $\dot{\varepsilon}$ is the strain rate (s^{-1}), σ is the flow stress at a strain of 1.0 (MPa), Q is the activation energy of deformation ($\text{kJ}\cdot\text{mol}^{-1}$), R is the gas constant ($8.3145 \text{ J}\cdot(\text{mol}\cdot\text{K})^{-1}$), T is the absolute temperature of deformation (K), and $\alpha = \beta/n_1$.

Taking the natural logarithms of both sides of Equations (1) and (2) gives the following:

$$\ln \dot{\varepsilon} = \ln A_1 - \frac{Q}{RT} + n_1 \ln \sigma \quad (4)$$

$$\ln \dot{\varepsilon} = \ln A_2 - \frac{Q}{RT} + \beta \sigma \quad (5)$$

According to Equations (4) and (5), the slopes of curve $\ln\dot{\epsilon}$ - $\ln\sigma$ and curve $\ln\dot{\epsilon}$ - σ can give the values of n_1 and β , respectively. Then, the value of α can be obtained by $\alpha = \beta/n_1$. In this paper, the peak stresses of the EBCHM Ti-6Al-4V alloy under different deformation conditions were used to construct the constitutive equation. The $\ln\dot{\epsilon}$ - $\ln\sigma$ and $\ln\dot{\epsilon}$ - σ graphs of EBCHM Ti-6Al-4V alloy within the used deformation temperature range are shown in Figures 3 and 4, respectively. The value of α was calculated as 0.021.

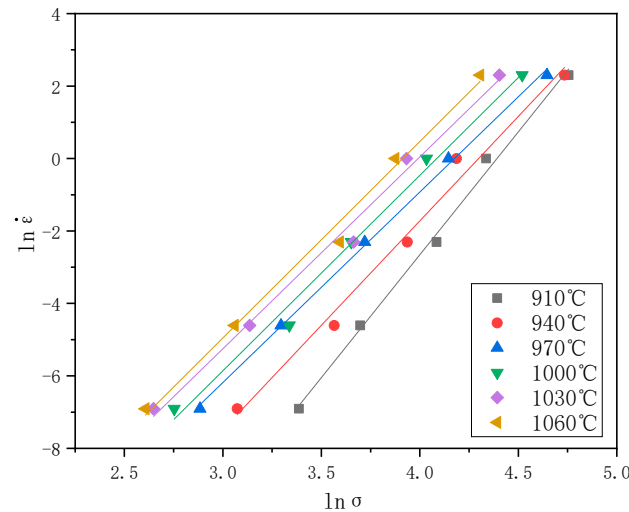


Figure 3. Linear fitting $\ln\dot{\epsilon}$ - $\ln\sigma$ diagram of the EBCHM Ti-6Al-4V alloy using the peak values of flow stresses under different deformation conditions.

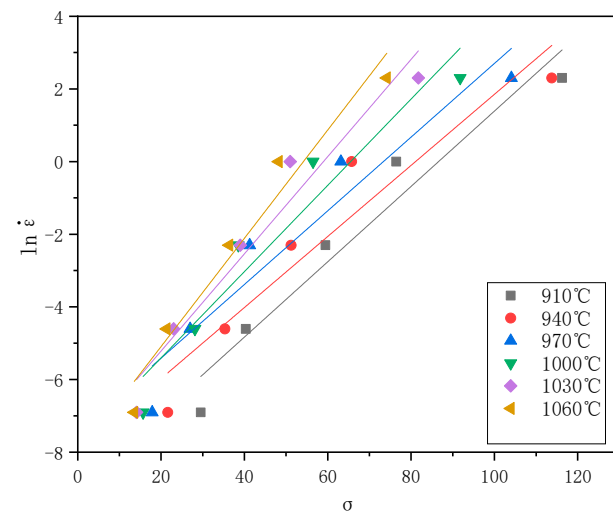


Figure 4. Linear fitting $\ln\dot{\epsilon}$ - σ diagram of the EBCHM Ti-6Al-4V alloy using the peak values of flow stresses under different deformation conditions.

Furthermore, taking the natural logarithms of both sides of Equation (3) gives the following:

$$\ln\dot{\epsilon} = \ln A - \frac{Q}{RT} + n \ln[\sinh(\alpha\sigma)] \tag{6}$$

Similarly, substitute the peak stress to draw the picture of $\ln\dot{\epsilon}$ - $\ln[\sinh(\alpha\sigma)]$, as shown in Figure 5. Using the linear fitting method, the value of n , which is the average slope of the fitting lines, was obtained as 4.165. It can be seen from the figure that the double logarithm of flow stress and strain rate satisfies the linear relationship. Therefore, it can be concluded that the stress–strain relationship of EBCHM Ti-6Al-4V alloy under high temperature compression deformation satisfies the hyperbolic sinusoidal form, and this

hyperbolic sinusoidal function relationship can be used to describe the relationship between flow stress and strain rate at the whole stress level of EBCHM Ti-6Al-4V alloy.

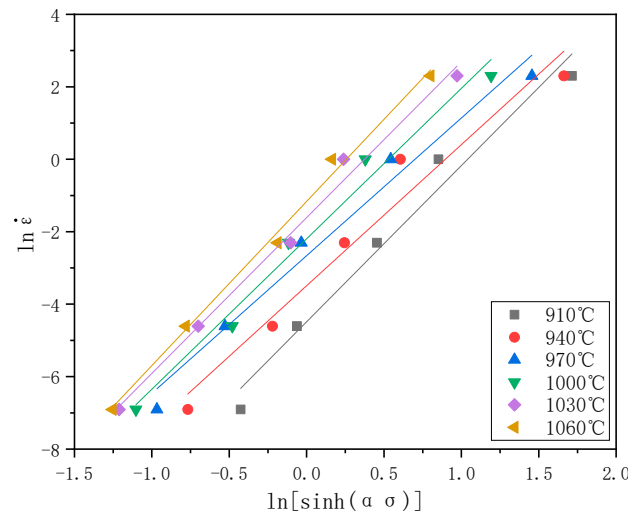


Figure 5. Linear fitting $\ln \dot{\epsilon} - \ln[\sinh(\alpha\sigma)]$ diagram of EBCHM Ti-6Al-4V alloy using the peak values of flow stresses under different deformation conditions.

The Equation (6) can be transformed as:

$$\ln[\sinh(\alpha\sigma)] = \frac{1}{n} \ln \dot{\epsilon} - \frac{1}{n} \ln A + \frac{Q}{nRT} \tag{7}$$

In drawing the picture of $\ln[\sinh(\alpha\sigma)] - 1/T$, we perform a linear regression on the data points, as shown in Figure 6. As can be seen from the figure, $\ln[\sinh(\alpha\sigma)]$ and $1/T$ are well consistent with the linear relationship in Equation (7), indicating that the flow stress and deformation temperature of the EBCHM Ti-6Al-4V alloy during high temperature deformation conform to the Arrhenius relationship. This relationship also indicates that the hot compression deformation of the EBCHM Ti-6Al-4V alloy is controlled by thermal activation. Taking the derivative of Equation (7) at a certain strain rate, we can obtain the following:

$$Q = Rn \frac{d \ln[\sinh(\alpha\sigma)]}{d \left(\frac{1}{T} \right)} \tag{8}$$

According to the above equation, $\ln[\sinh(\alpha\sigma)]$ is linear with $1/T$ when Q is independent of temperature. The slope of the $\ln[\sinh(\alpha\sigma)] - 1/T$ curve in Figure 6 was substituted into Equation (8) to obtain the deformation activation energy of the EBCHM Ti-6Al-4V alloy, which was found to be 277 kJ/mol. Since the calculated apparent activation energy value is close to the self-diffusion activation energy, the DRV controlled by the dislocation climb is supposed to be dominant in the hot deformation process.

To further estimate the comprehensive effect of temperature and strain rate on the deformation behavior, the Zener–Holloman parameter Z is calculated using the following equation:

$$Z = \dot{\epsilon} \exp \left(\frac{Q}{RT} \right) = A [\sinh(\alpha\sigma)]^n \tag{9}$$

Taking the natural logarithms of both sides of Equation (9) gives the following:

$$\ln Z = \ln A + n \ln [\sinh(\alpha\sigma)] \tag{10}$$

Then, using the same linear fitting method, as shown in Figure 7, the average intercept $\ln A$ and average slope n were obtained as 3.925 and 4.133, respectively. Therefore, the con-

stitutive equation of the EBCHM Ti-6Al-4V alloy during hot compression can be expressed as follows:

$$\dot{\epsilon} = e^{23.925} [\sinh(0.021\sigma)]^{4.133} \exp [-277226/(RT)] \tag{11}$$

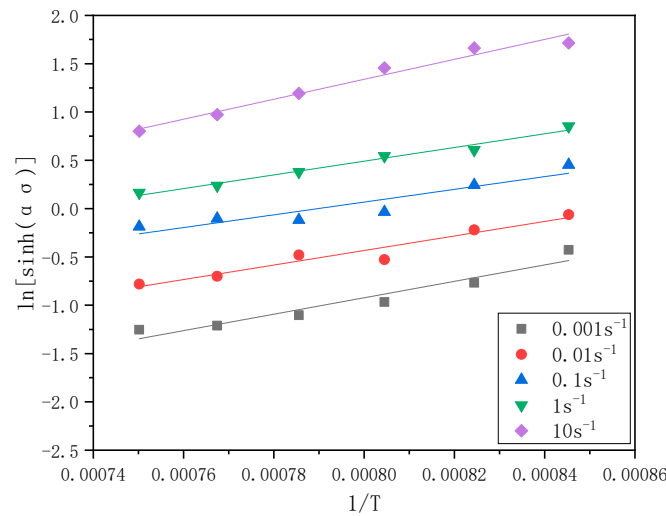


Figure 6. Linear fitting $\ln[\sinh(\alpha\sigma)]-1/T$ diagram of the EBCHM Ti-6Al-4V alloy using the peak values of flow stresses under different deformation conditions.

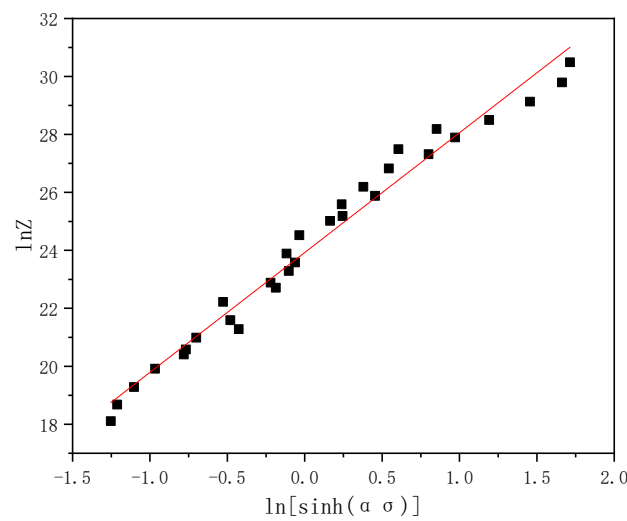


Figure 7. Linear fitting $\ln[\sinh(\alpha\sigma)]-1/T$ diagram of the EBCHM Ti-6Al-4V alloy using the peak values of flow stresses under different deformation conditions.

3.3. Processing Map

The hot processing map is an important index to characterize the plastic deformation ability of materials, and it is a powerful tool to optimize the production process. At present, the dynamic material model (DMM) proposed by Prasad et al. [25] is the most widely used and has been widely used with a variety of materials [26,27]. According to DMM, the thermal deformed workpiece can be regarded as a power dissipator, and the thermal deformation process can be regarded as a power dissipation process. During thermal deformation, part of the energy is dissipated through plastic deformation, which is represented by G , and the other part of energy is dissipated through microstructure evolution, represented by J . The corresponding power dissipation efficiency η can be used to reflect the mechanism of the microstructure evolution with a certain condition of deformation temperature and strain rate, which is defined as follows:

$$\eta = \frac{J}{J_{\max}} = \frac{2m}{m+1} \quad (12)$$

where J_{\max} can only be obtained at linear dissipation, in which case J is equal to G . Additionally, m is the strain rate sensitivity exponent, which is expressed as follows:

$$\eta = \frac{J}{J_{\max}} = \frac{2m}{m+1} \quad (13)$$

Based on the irreversible thermodynamic extremum principle of large plastic flow proposed by Zeigler, the Prasad instability criterion is established on the assumption that m is constant in the dynamic constitutive equation to identify the flow instable region in the processing maps. The Prasad flow instability parameter ξ is defined as follows:

$$\xi = \frac{\partial\{\lg[m/(m+1)]\}}{\partial(\lg\dot{\epsilon})} + m < 0 \quad (14)$$

Namely, flow instability will occur when ξ is negative. By superimposing the corresponding power dissipation (η) map and the (ξ) map, the processing maps of EBCHM Ti-6Al-4V alloy with true strain of 0.8 were obtained, as shown in Figure 8.

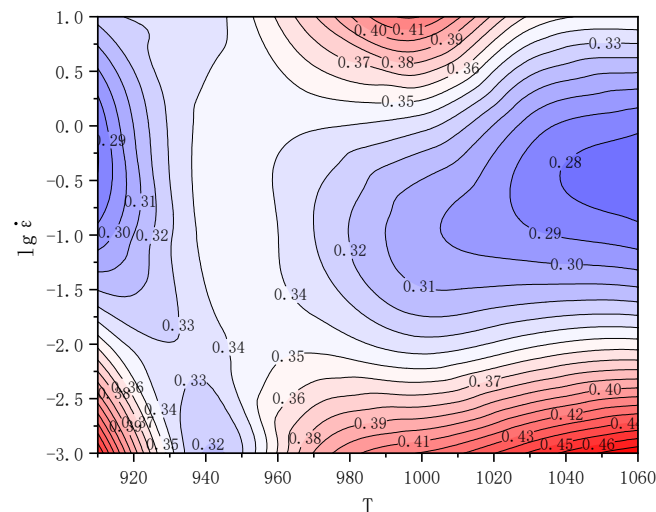


Figure 8. Processing map of the EBCHM Ti-6Al-4V alloy with the true strain of 0.8.

The processing map shows that the temperature and strain rate have a complicated effect on the hot deformation behavior of the EBCHM Ti-6Al-4V alloy. On the whole, there is no instability zone, indicating that the alloy is not prone to deformation and instability in the range of temperature and strain rate set by the experiment, and that it has a large processing window and good machinability. The lowest dissipation efficiency is obtained when the strain rate is medium at lower and higher temperatures. According to the DMM theory, regions with low dissipation efficiency have lower power for microstructure evolution and often correspond to regions with poor thermal working performance. These regions should be dominated by dynamic recovery without dynamic recrystallization. The peak dissipation efficiency is obtained when the strain rate is low at lower and higher temperatures, indicating that this alloy has better thermal working performance in this zone. Dynamic recrystallization should occur in these zones to make the deformation more adequate [21,28]. Under different conditions, different types of microstructure evolution of materials will affect their machinability, which is a common-sense law. In order to further understand the properties of materials, their microstructure evolution behavior needs to be explored.

3.4. Microstructure Evolution

Microstructure morphology is an important indicator to evaluate the hot deformation behavior of titanium alloy, and it is also critical for subsequent processes planning. In this paper, the microstructures for deformation in the single β phase field and $(\alpha + \beta)$ two-phase field will be analyzed, respectively. The microstructure evolution involved is mainly β phase in the single-phase field during the compression process, and the OM is used to analyze it. In the $(\alpha + \beta)$ two-phase deformation process, the microstructure evolution involved is α phase and β phase, and the EBSD is used for analysis.

3.4.1. Microstructure Evolution in the Single β Phase Field

Figure 9 presents the microstructure characteristics under typical deformation conditions in the single β phase field. Under the deformation condition of $1030\text{ }^{\circ}\text{C}/0.001\text{ s}^{-1}$, the microstructure contains a large number of recrystallized grains, suggesting that the β phase undergoes relatively sufficient dynamic recrystallization at a slower deformation rate, as shown in Figure 9a. Under the deformation condition of $1030\text{ }^{\circ}\text{C}/0.1\text{ s}^{-1}$, the characteristics of microstructure evolution are mainly dominated by elongated β grains, with a smaller number of recrystallizations. Under the deformation condition of $1030\text{ }^{\circ}\text{C}/10\text{ s}^{-1}$, uneven plastic deformation and shear bands can be observed. The difference in strain rate mainly leads to the difference in deformation time. When the deformation amount is 65%, the deformation times corresponding to the strain rates of 0.001, 0.1, and 10 s^{-1} are 1050, 10.5, and 0.105 s, respectively. When the deformation amount is sufficient, the slower strain rate enables the microstructure to have more adequate time for dynamic recrystallization, while the faster strain rate induces uneven plastic deformation. The law of microstructure evolution is consistent at other temperatures in the single β phase field. Moreover, the influence laws of process parameters on the evolution of the β phase are basically clear, and they will not be elaborated upon here.

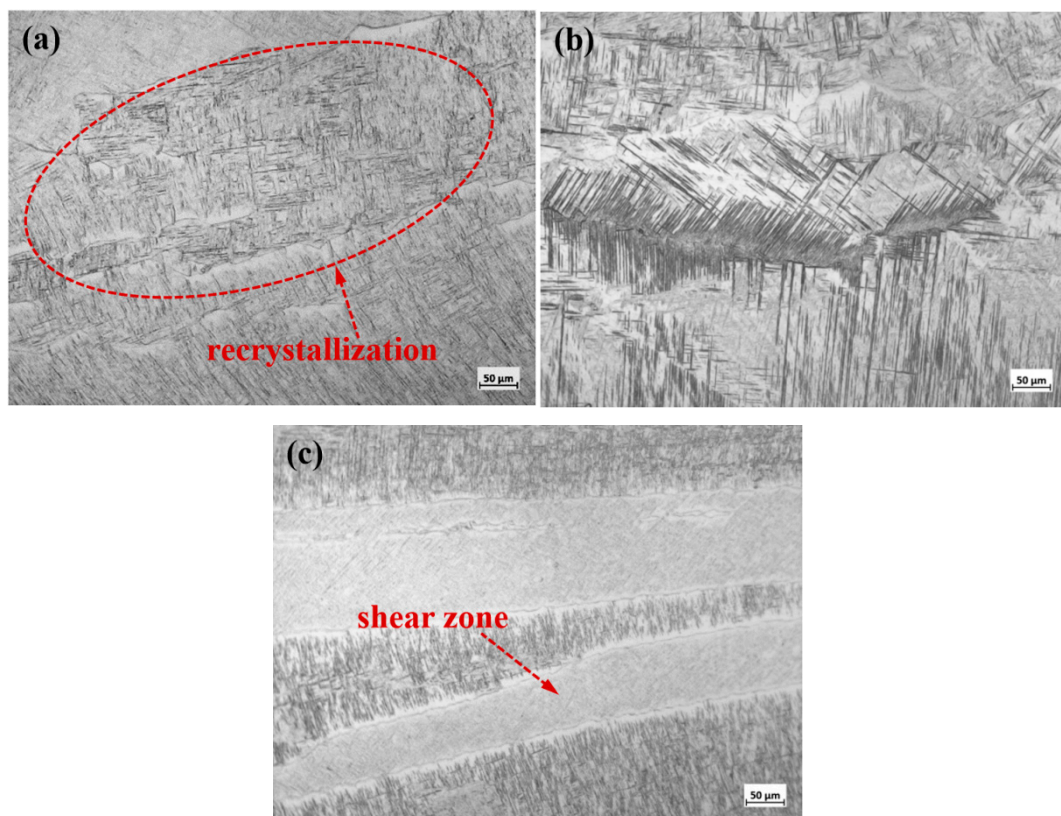


Figure 9. Microstructure characteristics under the deformation condition of the single β phase field: (a) $1030\text{ }^{\circ}\text{C}/0.001\text{ s}^{-1}$, (b) $1030\text{ }^{\circ}\text{C}/0.1\text{ s}^{-1}$, and (c) $1030\text{ }^{\circ}\text{C}/10\text{ s}^{-1}$.

3.4.2. Microstructure Evolution in the $\alpha + \beta$ Phase Field

According to the information obtained from the hot processing map, it can be found that the influence of temperature and strain rate on the hot deformation behavior of titanium alloy is comprehensive and complex. It is considered that this influence law is closely related to the characteristics of microstructure changes during the compression process. In the ($\alpha + \beta$) phase field, the microstructure evolution process is more complex due to the coexistence of the α phase and β phase, which involves not only the changes in microstructure morphology, but also the changes in crystallographic orientation and texture. In order to show the microstructure evolution characteristics in the ($\alpha + \beta$) phase region more clearly, the EBSD technology was used in this part.

Figure 10 shows crystallographic characteristics of microstructure with different strain rates at 910 °C. At a strain rate of 0.001 and 1 s⁻¹, the microstructure shows obvious deformation characteristics. The originally flat lamellar α phase becomes curved and twisted under the action of external forces, which is a typical globularization process. During this process, the crystallographic orientation of the microstructure changes differently and shows different colors. However, it can be seen that the orientations of the α phase are still similar in the same colony. At the strain rates of 0.001 and 1 s⁻¹, there is no significant difference in crystallographic orientation of microstructure. Moreover, significant texture characteristics of the [0001] vertical compression axis are presented due to the large deformation. Such texture characteristics are related to the prismatic slip of the α phase in the titanium alloy, which will be explained in detail by the Schmid factor. In contrast, the crystallographic characteristics of the microstructure are completely different when the strain rate is 10 s⁻¹, as shown in Figure 10(c1–c3). The microstructure does not show deformation characteristics; on the contrary, it shows a kind of precipitation characteristic. This is because the temperature rise caused by rapid deformation causes the temperature of the specimen to exceed the β transus temperature. This can also be reflected by the PF (pole figure), for which the precipitated α phase does not have obvious orientation concentration characteristics, and it can be seen that there are 12 variants. When the α phase is separated from the β phase, the α phase and β phase are related by the Burgers orientation relationship: $\{0001\}_\alpha // \{110\}_\beta$, $\langle 11\bar{2}0 \rangle_\alpha // \langle 111 \rangle_\beta$ [29,30]. Normally, 12 variants of the α phase will be precipitated. In the PF of $\{0001\}$, there are three points that are stronger, indicating that six variants are more abundant. Such a phenomenon indicates that the microstructure has some variant selection, which may be related to compression deformation [31–33].

Figure 11 shows the crystallographic characteristics of microstructure with different strain rates at 970 °C. In general, the microstructure also showed obvious globularization characteristics at a strain rate of 0.001 and 1 s⁻¹. However, the crystallographic orientation and texture characteristics show some differences compared with the sample at a temperature of 910 °C. At 970 °C, the orientation of the microstructure shows a certain dispersion characteristic, which is related to the higher deformation temperature. The higher deformation temperature causes the original α phase to dissolve, while the reprecipitated secondary α phase follows the Burgers orientation relationship, which leads to the increased dispersion of orientation. This phenomenon is especially obvious at the strain rate of 1 s⁻¹, because the rapid deformation increases the temperature of the sample. When the strain rate is increased to 10 s⁻¹, the temperature rise caused by rapid deformation causes the temperature of the sample to exceed the β transus temperature, and the α phase shows the characteristic of precipitation.

In addition, the grain size of the microstructure is significantly different when comparing samples at temperatures of 910 °C (Figure 10) and 970 °C (Figure 11). At 910 °C, the average grain size is about 2~4 μm ; by contrast, the average grain size is about 3~7 μm at 970 °C. Higher temperatures lead to the coarsening of the microstructure, which means there are fewer interfaces in the microstructure. This is one of the reasons for lower deformation stresses at higher temperatures.

For the α phase of titanium alloy, a dislocation slip is the main mode of deformation. In general, the α phase with a HCP (hexagonal close-packed) structure is the most likely

initiate an $\langle a \rangle$ type slip, that is, a slip in the $\langle a \rangle$ direction [11-20]. In order to better understand the behavior of the microstructure evolution, the Schmid factors of the basal $\{0001\}\langle 11-20 \rangle$, prismatic $\{1-100\}\langle 11-20 \rangle$, and pyramidal $\{1-101\}\langle 11-20 \rangle$ slip systems of α phase were analyzed, as shown in Figure 12. The larger the Schmid factor, the easier the slip is to initiate. Under different compression conditions, the Schmid factors of different slip systems show similar rules. The prismatic $\{1-100\}\langle 11-20 \rangle$ Schmid factor is the largest, while the basal $\{0001\}\langle 11-20 \rangle$ is second, and the pyramidal $\{1-101\}\langle 11-20 \rangle$ is the smallest. Hence, the prismatic slips occur more easily than basal and pyramidal slips. Such behavior is related to crystallographic structure of the α phase with the HCP structure. The activation of slip systems is influenced by the axial ratio (c/a). The basal slip occurs more easily when $c/a \geq 1.633$, or else the prismatic slip occurs more easily. The axial ration of the α phase of the titanium alloy is about 1.587; thus, the Schmid factor of the prismatic slip is larger [34].

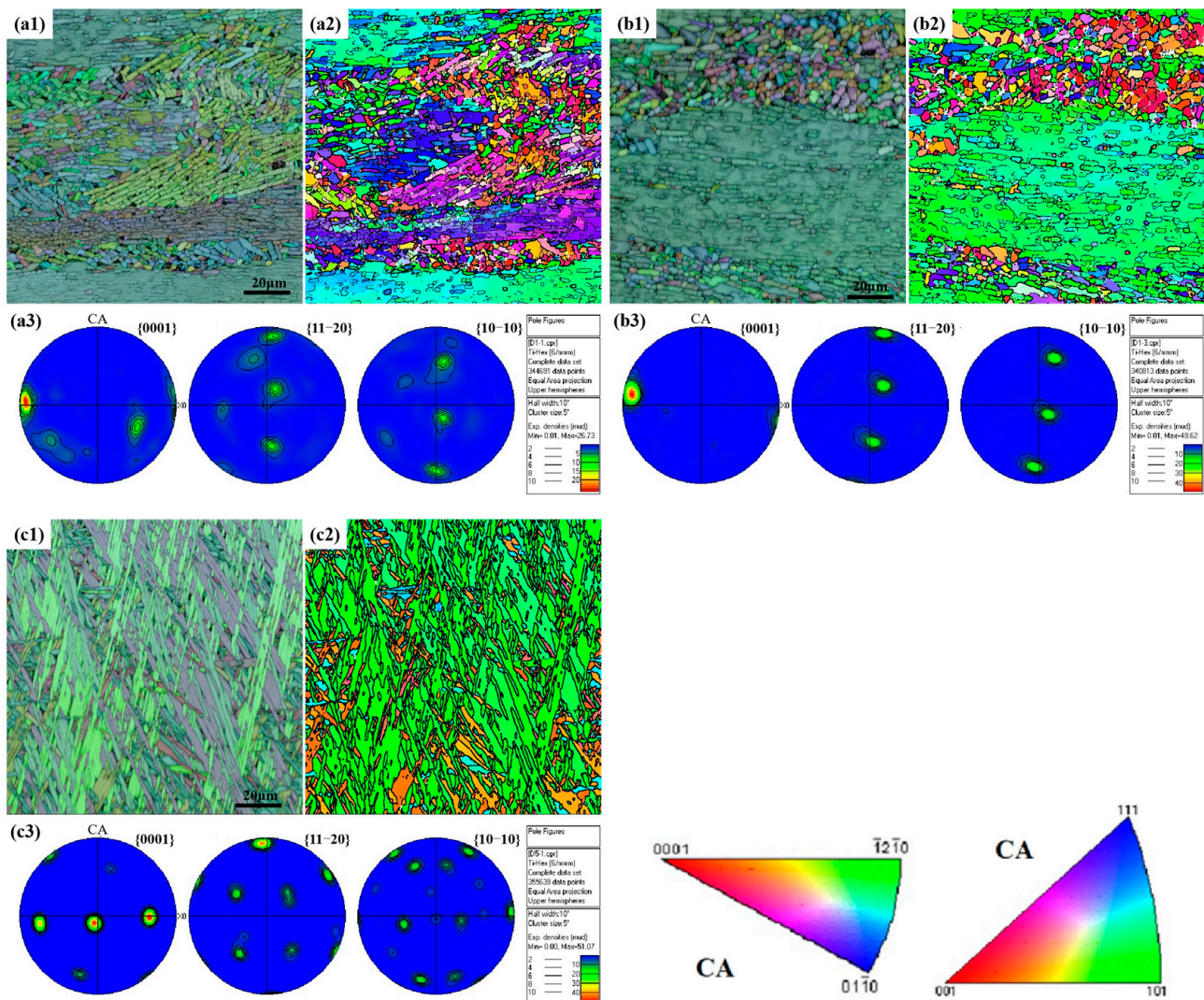


Figure 10. Euler + band contrast (BC) map, inverse pole figures (IPF), and pole figures (PF) of the microstructure at 910 °C: (a1) Euler + BC at a strain rate of 0.001 s^{-1} , (a2) IPF at a strain rate of 0.001 s^{-1} , (a3) PF at a strain rate of 0.001 s^{-1} , (b1) Euler + BC at a strain rate of 1 s^{-1} , (b2) IPF at a strain rate of 1 s^{-1} , (b3) PF at a strain rate of 1 s^{-1} , (c1) Euler + BC at a strain rate of 10 s^{-1} , (c2) IPF at a strain rate of 10 s^{-1} , and (c3) PF at a strain rate of 10 s^{-1} .

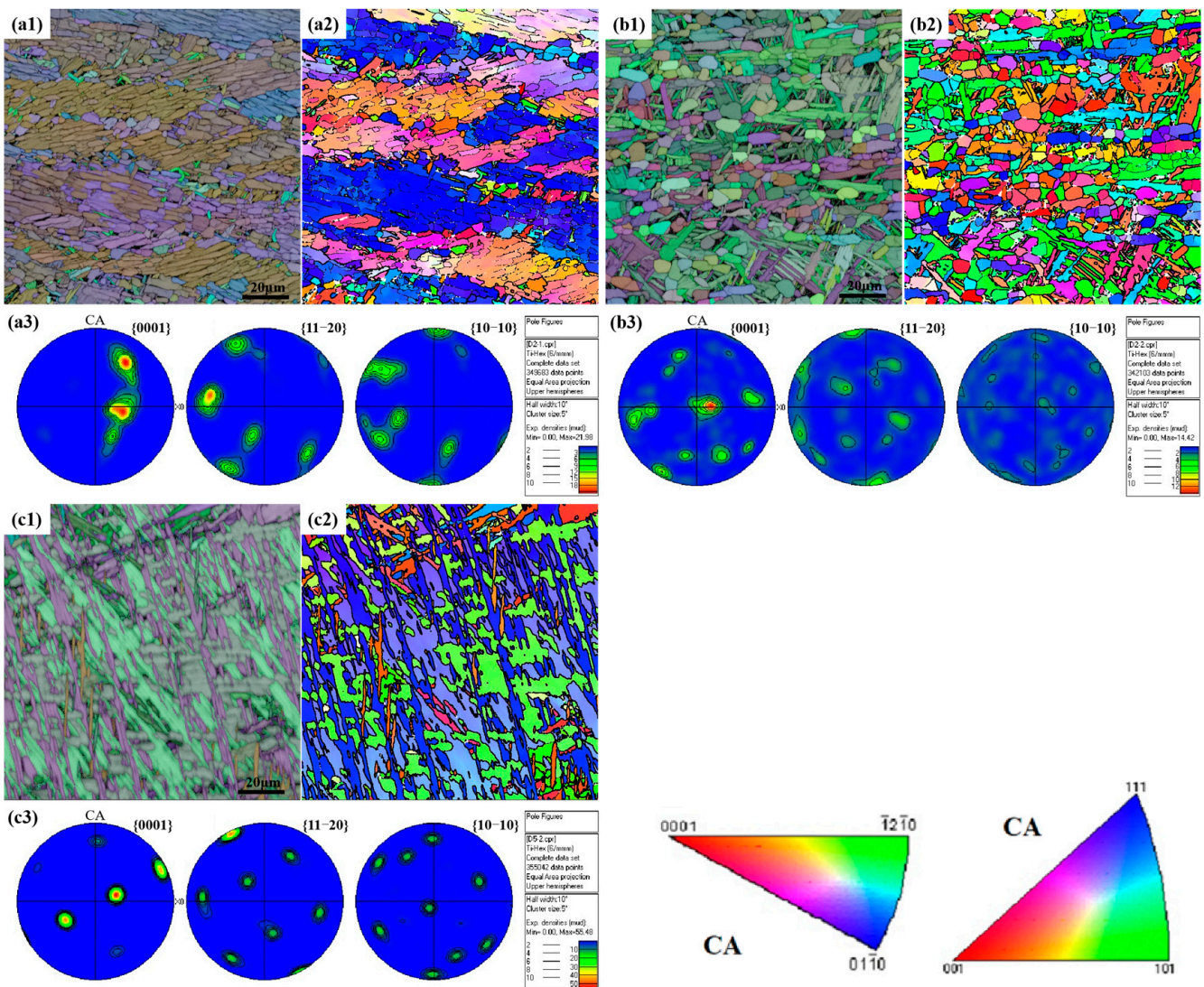


Figure 11. Euler + band contrast (BC) map, inverse pole figures (IPF), and pole figures (PF) of the microstructure at 970 °C: (a1) Euler + BC at a strain rate of 0.001 s^{-1} , (a2) IPF at a strain rate of 0.001 s^{-1} , (a3) PF at a strain rate of 0.001 s^{-1} , (b1) Euler + BC at a strain rate of 1 s^{-1} , (b2) IPF at a strain rate of 1 s^{-1} , (b3) PF at a strain rate of 1 s^{-1} , (c1) Euler + BC at a strain rate of 10 s^{-1} , (c2) IPF at a strain rate of 10 s^{-1} , and (c3) PF at a strain rate of 10 s^{-1} .

The globularization of the α phase is one of the main characteristics of the microstructure evolution during the deformation in the two-phase region. However, despite the large amount of deformation, some α phases still maintain the lamellar structure in morphology. In order to understand the globularization process more clearly, some typical α phases at $970 \text{ °C}/1 \text{ s}^{-1}$ are selected for targeted misorientation analysis, as shown in Figure 13. Some positions have a misorientation of more than 15° , such magnitudes represent the formation of high-angle boundary. Therefore, these α phases have completed the globularization process in crystallography. However, they have not yet completed the morphological separation due to insufficient time. After heat treatment, these high-angle boundaries will be separated quickly, and the globularization process in morphology will be completed.

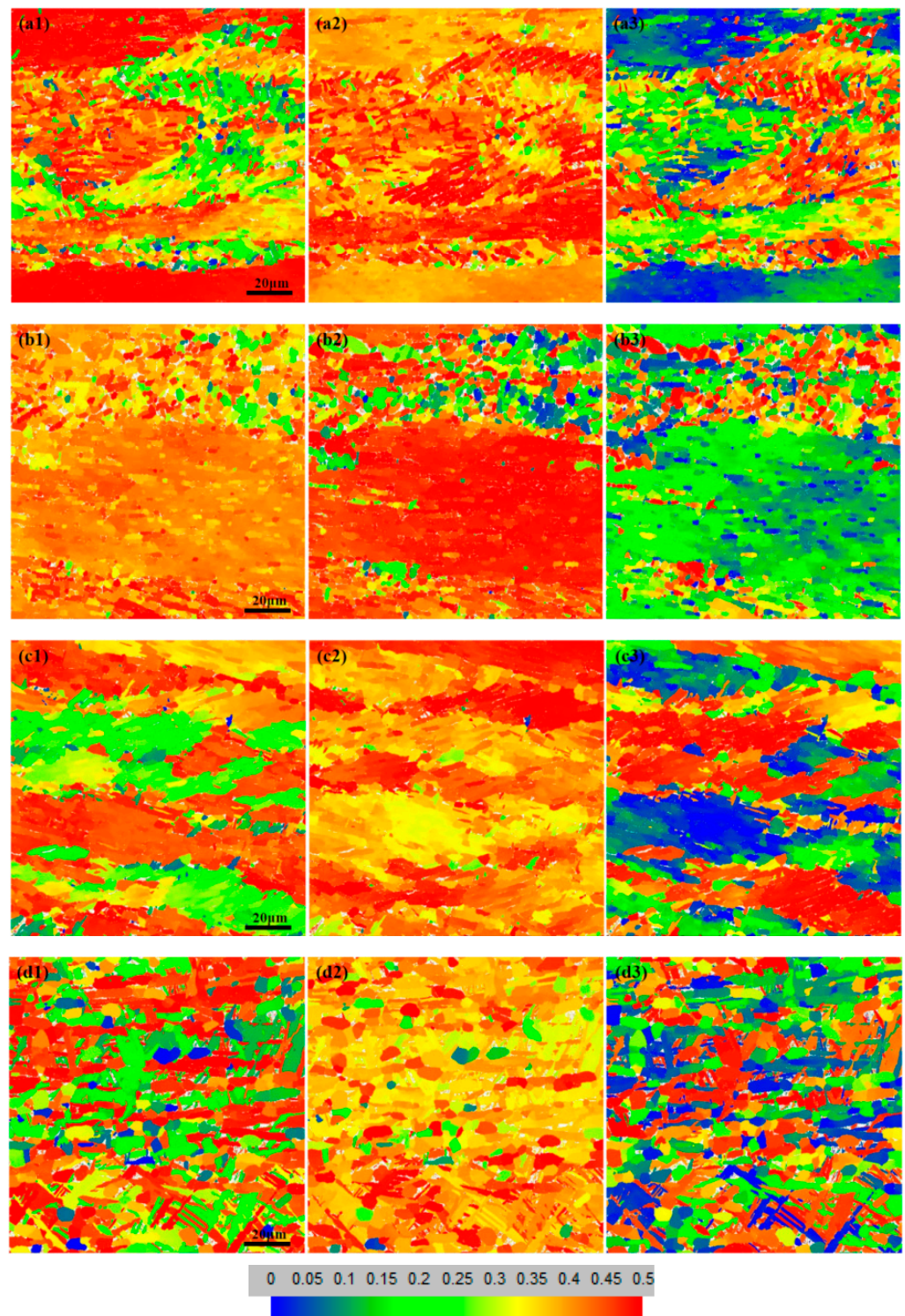


Figure 12. Schmid factor maps for different slip systems at 910 °C (a,b) and 970 °C (c,d): (a1) (0001)<11-20> at a strain rate of 0.001 s^{-1} , (a2) (1-100)<11-20> at a strain rate of 0.001 s^{-1} , (a3) (1-101)<11-20> at a strain rate of 0.001 s^{-1} , (b1) (0001)<11-20> at a strain rate of 1 s^{-1} , (b2) (1-100)<11-20> at a strain rate of 1 s^{-1} , (b3) (1-101)<11-20> at a strain rate of 1 s^{-1} , (c1) (0001)<11-20> at a strain rate of 0.001 s^{-1} , (c2) (1-100)<11-20> at a strain rate of 0.001 s^{-1} , (c3) (1-101)<11-20> at a strain rate of 0.001 s^{-1} , (d1) (0001)<11-20> at a strain rate of 1 s^{-1} , (d2) (1-100)<11-20> at a strain rate of 1 s^{-1} , and (d3) (1-101)<11-20> at a strain rate of 1 s^{-1} .

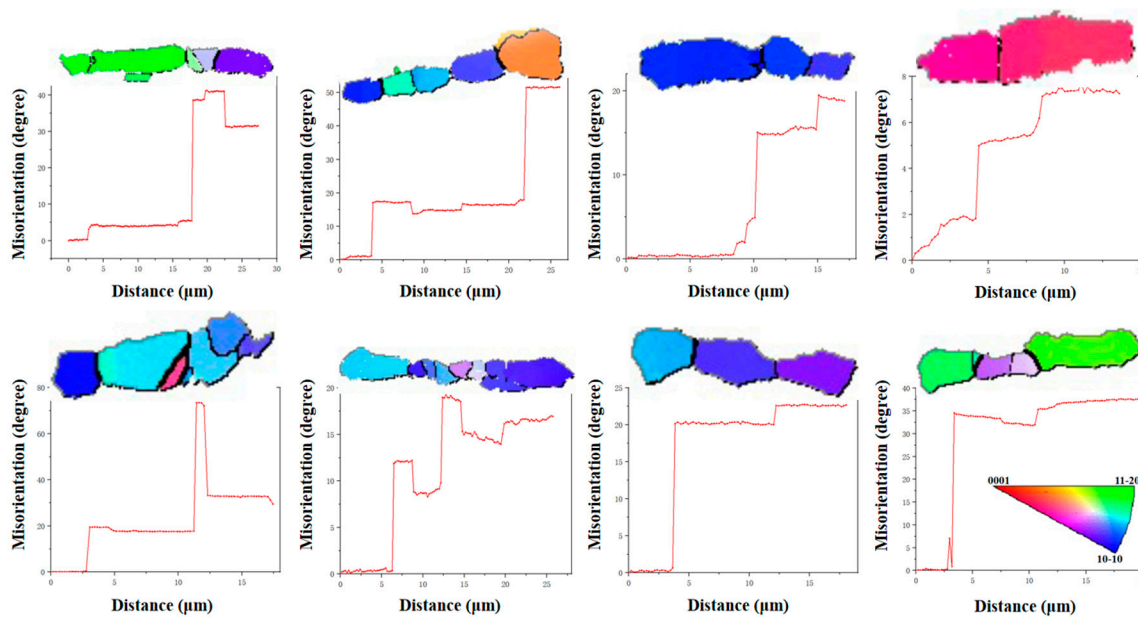


Figure 13. Crystallographic characteristics of the typical α phase at $970\text{ }^{\circ}\text{C}/1\text{ s}^{-1}$.

4. Conclusions

In the current work, the deformation behavior and microstructure changes of electron-beam cold-hearth-melted Ti-6Al-4V alloy were investigated. The main conclusions are as follows:

- (1) The stress–strain curves of electron-beam cold-hearth-melted Ti-6Al-4V alloy for isothermal compression in the $\alpha + \beta$ and single β phase fields were obtained. The constitutive model was established based on the classical Arrhenius equation. In addition, a hot processing map was drawn, and it is a powerful tool to optimize the production process.
- (2) Microstructure evolution in the single β phase field presents different characteristics with the change in strain rate. When the strain rate is slow, there are more recrystallized grains, and the recrystallization of the β phase does not have enough time to occur when the strain rate is fast. At the strain rate of 10 s^{-1} , there are obvious shear bands in the microstructure.
- (3) Microstructure evolution in the $\alpha + \beta$ phase field is more complicated. The morphology and crystallographic orientation of the microstructure changed simultaneously. Globularization is a typical microstructure evolution characteristic, which occurs mainly through dislocation slips. The Schmid factor of the prismatic $\{1-100\}\langle 11-20\rangle$ slip is largest, the basal $\{0001\}\langle 11-20\rangle$ slip is second, and the pyramidal slip $\{1-101\}\langle 11-20\rangle$ is the smallest. Prismatic slips are easier to activate than basal and pyramidal slips. Moreover, globularization of the lamellar α phase is not synchronously crystallographic and morphological.

Author Contributions: Conceptualization, W.J.; methodology, W.J. and C.M.; formal analysis, W.J., C.M. and W.Z.; investigation, W.J. and C.M.; resources, W.Z.; data curation, C.M. and W.Z.; writing—original draft preparation, W.J.; writing—review and editing, W.J.; funding acquisition, W.J. All authors have read and agreed to the published version of the manuscript.

Funding: This research was funded by the Construction of ‘Scientists + Engineers’ Team in Qinchuangyuan, Shaanxi Province, grant number 2022KXJ-079.

Data Availability Statement: The raw data supporting the conclusions of this article will be made available by the authors on request.

Conflicts of Interest: Authors Weiju Jia, Chengliang Mao and Wei Zhou were employed by the company Northwest Institute for Nonferrous Metal Research. The remaining authors declare that the research was conducted in the absence of any commercial or financial relationships that could be construed as a potential conflict of interest.

References

1. Leyens, C.; Peters, M. *Titanium and Titanium Alloys*; Wiley-VCH: Weinheim, Germany, 2003; p. 513.
2. Boyer, R.R. An overview on the use of titanium in the aerospace industry. *Mater. Sci. Eng. A* **1996**, *213*, 103–114. [[CrossRef](#)]
3. Zhang, Y.; Zhou, L.; Sun, J.; Han, M.; Georg, R.; Jochen, F.; Yang, J.; Zhao, Y. An Investigation on electron beam cold hearth melting of Ti64 alloy. *Rare Met. Mater. Eng.* **2008**, *37*, 1973–1977. [[CrossRef](#)]
4. Motrunich, S.; Berezos, V.; Kostin, V.; Klochkov, I.; Akhonin, D. Fatigue behavior and fracture of medical Ti-6Al-7Nb titanium alloy produced by electron beam cold hearth melting. *Procedia Struct. Integr.* **2024**, *59*, 58–65. [[CrossRef](#)]
5. Liu, Q.; Li, X.; Jiang, Y. Numerical simulation of EBCHM for the large-scale TC4 alloy slab ingot during the solidification process. *Vacuum* **2017**, *141*, 1–9. [[CrossRef](#)]
6. Momeni, A.; Abbasi, S.M. Effect of hot working on flow behavior of Ti-6Al-4V alloy in single phase and two phase regions. *Mater. Des.* **2010**, *31*, 3599–3604. [[CrossRef](#)]
7. Jha, J.S.; Tewari, A.; Mishra, S.; Toppo, S. Constitutive Relations for Ti-6Al-4V Hot Working. *Procedia Eng.* **2017**, *173*, 755–762. [[CrossRef](#)]
8. Ji, X.; Guo, B.; Jiang, F.; Yu, H.; Fu, D.; Teng, J.; Zhang, H.; Jonas, J.J. Accelerated flow softening and dynamic transformation of Ti-6Al-4V alloy in two-phase region during hot deformation via coarsening α grain. *J. Mater. Sci. Technol.* **2020**, *36*, 160–166. [[CrossRef](#)]
9. Cai, J.; Wang, K.; Han, Y. A Comparative study on Johnson Cook, Modified Zerilli-Armstrong and Arrhenius-Type constitutive models to predict high-temperature flow behavior of Ti-6Al-4V alloy in $\alpha+\beta$ Phase. *J. Mater. Eng. Perform.* **2016**, *35*, 1952–1963. [[CrossRef](#)]
10. Wanjara, P.; Jahazi, M.; Monajati, H.; Yue, S.; Immarigeon, J.P. Hot working behavior of near- α alloy IMI834. *Mater. Sci. Eng. A* **2005**, *396*, 50–60. [[CrossRef](#)]
11. Chuan, W.; Liang, H. Hot deformation and dynamic recrystallization of a near-beta titanium alloy in the β single phase region. *Vacuum* **2018**, *156*, 384–401. [[CrossRef](#)]
12. Su, Y.; Kong, F.; You, F.; Wang, X.; Chen, Y. The high-temperature deformation behavior of a novel near- α titanium alloy and hot-forging based on the processing map. *Vacuum* **2020**, *173*, 109135. [[CrossRef](#)]
13. Ma, X.; Zeng, W.D.; Tian, F.; Zhou, Y.G. The kinetics of dynamic globularization during hot working of a two phase titanium alloy with starting lamellar microstructure. *Mater. Sci. Eng. A* **2012**, *548*, 6–11. [[CrossRef](#)]
14. Park, C.H.; Won, J.W.; Park, J.W.; Semiatin, S.L.; Lee, C.S. Mechanisms and kinetics of static spheroidization of hot-worked Ti-6Al-2Sn-4Zr-2Mo-0.1Si with a lamellar microstructure. *Metall. Mater. Trans. A* **2012**, *43*, 977–985. [[CrossRef](#)]
15. Lin, Y.C.; Pang, G.; Jiang, Y.; Liu, X.; Zhang, X.; Chen, C.; Zhou, K. Hot compressive deformation behavior and microstructure evolution of a Ti55511 alloy with basket-weave microstructures. *Vacuum* **2019**, *169*, 108878. [[CrossRef](#)]
16. Wang, K.; Wu, M.-Y.; Ren, Z.; Zhang, Y.; Xin, R.-L.; Liu, Q. Static globularization and grain morphology evolution of α and β phases during annealing of hot-rolled TC21 titanium alloy. *Trans. Nonferrous Met. Soc. China* **2021**, *31*, 2664–2676. [[CrossRef](#)]
17. Wang, L.; Fan, X.G.; Zhan, M.; Jiang, X.Q.; Liang, Y.F.; Zheng, H.J.; Liang, W.J. Revisiting the lamellar globularization behavior of a two-phase titanium alloy from the perspective of deformation modes. *J. Mater. Process. Technol.* **2021**, *289*, 116963. [[CrossRef](#)]
18. Balachandran, S.; Kumar, S.; Banerjee, D. On recrystallization of the α and β phases in titanium alloys. *Acta Mater.* **2017**, *131*, 423–434. [[CrossRef](#)]
19. Xu, J.; Zeng, W.; Jia, Z.; Sun, X.; Zhou, J. Static globularization kinetics for Ti-17 alloy with initial lamellar microstructure. *J. Alloys Compd.* **2014**, *603*, 239–247. [[CrossRef](#)]
20. Xu, J.; Zeng, W.; Ma, H.; Zhou, D. Static globularization mechanism of Ti-17 alloy during heat treatment. *J. Alloys Compd.* **2018**, *736*, 99–107. [[CrossRef](#)]
21. Seshacharyulu, T.; Medeiros, S.C.; Morgan, J.T.; Malas, J.C.; Frazier, W.G.; Prasad, Y.V.R.K. Hot deformation and microstructural damage mechanisms in extra-low interstitial (ELI) grade Ti-6Al-4V. *Mater. Sci. Eng. A* **2000**, *279*, 289–299. [[CrossRef](#)]
22. Zeng, W.D.; Shu, Y.; Zhang, X.M.; Zhou, Y.G.; Zhao, Y.Q.; Wu, H.; Dai, Y.; Yang, J.; Zhou, L. Hot workability and microstructure evolution of highly beta stabilised Ti-25V-15Cr-0.2Si alloy. *Mater. Sci. Technol.* **2008**, *24*, 1222–1229. [[CrossRef](#)]
23. Li, A.B.; Huang, L.J.; Meng, Q.Y.; Geng, L.; Cui, X.P. Hot working of Ti-6Al-3Mo-2Zr-0.3Si alloy with lamellar $\alpha+\beta$ starting structure using processing map. *Mater. Des.* **2009**, *30*, 1625–1631. [[CrossRef](#)]
24. Sellars, C.M.; McTegart, W.J. On the mechanism of hot deformation. *Acta Metall.* **1966**, *14*, 1136–1138. [[CrossRef](#)]
25. Prasad, Y.V.R.K.; Gegel, H.L.; Doraivelu, S.M. Modeling of dynamic metal behavior in hot deformation forging of Ti-6242. *Metall. Trans. A* **1984**, *15*, 1883–1892. [[CrossRef](#)]
26. Prasad, Y.V.R.K.; Seshacharyulu, T. Processing maps for hot working of titanium alloys. *Mater. Sci. Eng. A* **1998**, *243*, 82–88. [[CrossRef](#)]
27. Zeng, W.D.; Zhou, Y.G.; Zhou, J.; Yu, H.Q.; Zhang, X.M.; Xu, B. Recent development of processing map theory. *Rare Met. Mater. Eng.* **2006**, *35*, 673–677.

28. Peng, X.; Guo, H.; Shi, Z.; Qin, C.; Zhao, Z.; Yao, Z. Study on the hot deformation behavior of TC4-DT alloy with equiaxed $\alpha+\beta$ starting structure based on processing map. *Mater. Sci. Eng. A* **2014**, *605*, 80–88. [[CrossRef](#)]
29. Zhao, Z.B.; Wang, Q.J.; Liu, J.R. Effect of heat treatment on the crystallographic orientation evolution in a near- α titanium alloy Ti60. *Acta Mater.* **2017**, *131*, 305–314. [[CrossRef](#)]
30. Xu, J.; Hu, W.; Ji, X.; Zeng, W. Evolution characteristics of orientation relationships during the co-evolution of α/β phase for Ti alloy. *Mater. Charact.* **2023**, *203*, 113111. [[CrossRef](#)]
31. Shi, R.; Dixit, V.; Viswanathan, G.B.; Fraser, H.L.; Wang, Y.J.A.M. Experimental assessment of variant selection rules for grain boundary alpha in titanium alloys. *Acta Mater.* **2016**, *102*, 197–211. [[CrossRef](#)]
32. Qiu, D.; Zhao, P.; Shi, R.; Wang, Y.; Lu, W. Effect of autocatalysis on variant selection of α precipitates during phase transformation in Ti-6Al-4V alloy. *Comput. Mater. Sci.* **2016**, *124*, 282–289. [[CrossRef](#)]
33. Xu, J.; Zeng, W.; Zhu, Z.; Li, M.; Du, J.; He, S.; Wang, X. Precipitation and evolution behaviors of grain boundary α and α side plates for ultra-high strength titanium alloy during continuous cooling. *Mater. Des.* **2023**, *225*, 111562. [[CrossRef](#)]
34. Xu, J.; Zeng, W.; Zhou, D.; Chen, W.; He, S.; Zhang, X. Analysis of crystallographic orientation and morphology of microstructure during hot working for an alpha/beta titanium alloy. *J. Mater. Sci. Technol.* **2020**, *59*, 1–13. [[CrossRef](#)]

Disclaimer/Publisher’s Note: The statements, opinions and data contained in all publications are solely those of the individual author(s) and contributor(s) and not of MDPI and/or the editor(s). MDPI and/or the editor(s) disclaim responsibility for any injury to people or property resulting from any ideas, methods, instructions or products referred to in the content.